Catalysis Today 372 (2021) 154–163

Contents lists available at ScienceDirect

Catalysis Today

journal homepage: www.elsevier.com/locate/cattod

Use of PdCu catalysts supported on zirconia-ceria based supports for the elimination of oxyanions present in water

Marisa B. Navas [a], Hernán P. Bideberrripe [a], Carmen I. Cabello [a,b,c], Delia Gazzoli [d], Mónica L. Casella [a], María A. Jaworski [a,b,*]

[a] Centro de Investigación y Desarrollo en Ciencias Aplicadas "Dr. Jorge J. Ronco" (CINDECA), CCT-CONICET La Plata, Universidad Nacional de la Plata and Comisión de Investigaciones Científicas de la Provincia de Buenos Aires (CICPBA), calle 47 N° 257, 1900 La Plata, Argentina
[b] Facultad de Ingeniería, Universidad Nacional de La Plata, calle 1 y 47, 1900 La Plata, Argentina
[c] Miembro CIC, Comisión de Investigaciones Científicas y Técnicas, Provincia de Buenos Aires, Argentina
[d] Dipartimento di Chimica, La Sapienza Università di Roma, Piazzale Aldo Moro 5, I-00185 Roma, Italy

ARTICLE INFO

Keywords:
CeO_2, Nitrate
Nitrite
Bromate
CeO_2-ZrO_2 support

ABSTRACT

In the present work, the elimination of NO_3^-, NO_2^- and BrO_3^- in distilled and groundwater samples using H_2 as reducing agent is studied. For this purpose, PdCu-based catalysts were prepared on CeO_2 pure and modified with 10 % of ZrO_2 supports. The prepared catalysts were characterized by N_2 physisorption, SEM-EDS, XRD, TPR, RAMAN, FTIR and XPS. The results showed that the materials obtained were mesoporous, exposing the cubic CeO_2 crystalline phase. Raman and FTIR analysis allow corroborating that both supports have oxygen vacancies, being higher in the ZrCe support, due to the presence of Zr^{4+} ions in the CeO_2 lattice. All the prepared catalysts were active in the elimination of the selected oxyanions, showing high selectivities (>99 %) towards the product of interest (N_2 and Br^-), especially the catalyst PdCu/10ZrCe. This catalyst presented the highest oxyanion removal rate, which is higher for NO_3^- elimination ($V_{0,NO3-}$: 5.6; $V_{0,BrO3-}$:.0.93). In the reduction stage, Ce^{4+} is reduced to Ce^{3+}, generating oxygen vacancies at the metal-support interface. It is postulated that the reduction of the anions occurs by interaction of the oxygen atoms of the NO_3^-, NO_2^- or BrO_3^- species with the oxygen-vacant sites generated. The addition of Zr on ceria support increases its ability to activate anions and reduce them. PdCu/10ZrCe catalyst was also tested using groundwater. The conversion results obtained were promising, 60 % for NO_2^-, 70 % for NO_3^- and 27 % for BrO_3^-.

1. Introduction

There is a variety of compounds that affect the quality of water destined for human consumption, among them there are various oxyanions, including NO_3^-, NO_2^-, BrO_3^-, ClO_3^- and ClO_4^-. Agricultural and livestock activities produce discharges of pesticides, fertilizers and organic remains of animals and plants. These wastes pollute notoriously water, in particular groundwater. One of the main problems generated is the high concentration levels of NO_3^- and NO_2^- [1–3]. When the levels of NO_3^- in the soil are greater than that which the plants can assimilate, the irrigation and rainwater cause that NO_3- percolate and reach groundwater layers [4]. Excess intake of NO_3^- ions can cause serious health problems, due to the fact that NO_3- is easily transformed to NO_2^- in the human body. This causes an oxygen deficiency in the blood, mainly in children, called methemoglobinemia [4,5]. In addition, NO_2- are precursors of carcinogenic nitrosamines [6].For this reason, maximum tolerable limits have been established for these anions through different legislations [7–9] in water for human consumption. The maximum limit level of NO_3^- by the World Health Organization is 50 mg/L in the water supply for the population. In Argentina, the Food Code established a maximum concentration of NO_3^- of 45 ppm. In Buenos Aires province (Argentina), the Puelche aquifer extends uninterruptedly in the subsoil, occupying approximately 89,000 km^2. This aquifer is highly exploited both for irrigation and for human consumption and the potability is affected by the NO_3^- content, particularly in urbanized areas [2,10].

The disinfection of water for human consumption is achieved mainly by ClO^- addition. However, as this method generates halogenated byproducts, an alternative method is the ozonation [11]. The ozonation process improves the taste of water, but can allow the formation of BrO_3^-, a potentially toxic byproduct. BrO_3^- is formed from the reaction

* Corresponding author.
E-mail address: majaworski@quimica.unlp.edu.ar (M.A. Jaworski).

https://doi.org/10.1016/j.cattod.2020.08.012
Received 30 March 2020; Received in revised form 9 July 2020; Accepted 20 August 2020
Available online 1 September 2020
0920-5861/Published by Elsevier B.V.

between ozone radicals and ˙OH [12], through many intermediates. Besides, BrO_3^- is also naturally formed as a byproduct of surface bromide oxidation, particularly in saltwater [11].

BrO_3^- is classified as a Group 2B human potential carcinogen by the International Agency for Research on Cancer (IARC). This is due to the induction of tumours in rats and mice, but there is lack of evidence of carcinogenicity in humans. Different legislations have been established a maximum level of BrO_3^- of 10 μg/mL in human consumption water [7–9].

There are different treatments for the elimination of the excess of oxyanions in drinking water such as ion exchange and reverse osmosis, but both techniques need a water pre-treatment, to preserve the membranes [13]. These methods also accumulate anions and do not eliminate them. For that reason, the best technique to remove these anions is to transform them into innocuous products: NO_3^- to N_2, ClO_4^- to Cl^-, BrO_3^- to Br^-. For example, when biological denitrification is applied, the microorganisms transform NO_3- to N_2. Nevertheless, this technique presents problems such as incomplete degradation of organic compounds or the need for pre-treatment [13].

One of the most promising processes is the catalytic reduction of these oxyanions to harmless products using a reducing agent as H_2 [14, 15]. Generally, the employed catalysts contain a precious metal as a base (Pd, Rh, Ru or Pt), and a metal acting as a promoter (Cu, Ag, Fe, Hg, Ni, Cu, Zn, Sn or In) [16,17]. In these catalysts, the bimetallic sites allow the reduction of NO_3^- to NO_2^-, which then are reduced to N_2.

In the last years, many catalysts have been synthesized for the reduction of different oxyanions, presenting high activity in the reactions studied [18–20]. There are numerous bibliographical references that show the influence of the support on the activity and selectivity in the hydrogenation reactions. For example, Pd-based catalysts supported on SBA-15 and SBA-15-modified CeO_2, prepared by impregnation, or by strong electrostatic adsorption (Ce-SBA-15), were tested in BrO_3^- removal [21]. When the catalysts were prepared by electrostatic adsorption, a higher Pd dispersion and a stronger interaction with the support were observed. The same effect was achieved by increasing the amount of CeO_2 and decreasing the amount of Pd on the catalyst. The highest catalytic activity was observed for Pd catalysts supported on Ce-SBA-15 [22].

Metal oxides are of interest in different fields, such as catalysis, biochemical engineering or environmental remediation. Materials containing ceria have a wide range of applications, due to its redox behavior, and can be used as oxygen storage/release material [22,23]. CeO_2 has a significant oxygen storage capacity (OSC), and also, is a good material to stabilize the dispersion of precious metals, such as Pt, Pd and Rh. For this reason, ceria is used in three-way catalysts [24–26]. Several studies have demonstrated that CeO_2 can be modified, adding dopants, like Zr^{4+}, La^{3+} or Eu^{3+} [27,28]. These dopants modify the lattice strain, the oxygen vacancy sites, and therefore, the physicochemical properties. The dopants introduce modifications in the fluorite-type lattice: increased lattice strain and more oxygen vacancy sites, for example. This causes an increment in the Oxygen Storage Capacity (OSC) of the mixed oxide. This modification improves the catalytic performance in reactions such as Water Gas Shift, hydrocarbon steam reforming, and CO oxidation [29]. Adding zirconium into CeO_2 generates more oxygen vacancies, so these materials have better OSC and thermal stability [30, 31]. Besides, Zr addition provides better catalytic activity at lower temperatures than CeO_2 [30]. It was found in literature that Pd-catalysts, prepared on redox supports or supports with oxygen vacancies, such as ZrO_2, CeO_2 or TiO_2, presented high activity in NO_3^- elimination, and also high selectivity to the desired product N_2 [32,33]. In these catalysts, new NO_3^- adsorption sites are generated, due to the presence of oxygen vacancies. These vacancies sites, close to Pd sites, would allow the activation of NO_3 sites.

There are different methods for the preparation of Ce-Zr mixed oxides, like hydrothermal synthesis, sol-gel methods or surfactants-assisted methods [34]. Among them, the sol-gel method is usually preferred, due to its many advantages, like high homogeneity, a lower number of process steps, and soft conditions. This method allows synthesizing particles with controlled size [35]. Materials with different compositions of Ce and Zr can be prepared, obtaining different degrees of homogeneity and textural properties.

As a contribution on the subject, the purpose of this work is to synthesize and characterize PdCu-based heterogeneous catalysts for environmental remediation of contaminated water. Pure and Zr-modified ceria were the selected supports. These catalysts were tested in the removal of NO_3^-, NO_2^- and BrO_3^- anions present in distilled and groundwater.

2. Materials and methods

2.1. Support preparation

The supports were prepared using the precipitation and co-precipitation method. $(NH_4)_2Ce(NO_3)_6$ and $ZrOCl_2.8H_2O$ (*Fluka*) were employed as source of Ce and Zr respectively. The precursor salts were dissolved in distillated water in an appropriate concentration so as to obtain pure ceria or 10 wt% ZrO_2 on CeO_2. Concentrated NH_4OH was added to these solutions slowly under constant stirring. The obtained solids were aged for 1 day, dried overnight at 105 °C and finally calcined at 600 °C for 2 h. The prepared supports were named as CeO_2 and 10ZrCe.

2.2. Catalyst preparation

The Pd-based catalysts (1 wt%) were prepared by impregnating the supports with a solution of H_2PdCl_4 prepared from $PdCl_2$ (*Sigma–Aldrich*) in HCl (pH = 1). The solids obtained were dried at 105 °C and calcined in air at 400 °C. After that, the monometallic catalysts prepared were impregnated with a solution of $Cu(NO_3)_2$ (*Merck*), so as to obtain 0.3 wt% Cu on the solid. The bimetallic catalyst was first dried at 105 °C and then calcined at 400 °C. The prepared catalysts were named as $PdCu/CeO_2$ and PdCu/10ZrCe.

2.3. Catalysts characterization

The total surface area of the prepared supports was obtained by the Brunauer-Emmer-Teller (BET) method, using N_2 physisorption at 77 K, with a Micromeritics ASAP 2020 analyzer. The pore volume (Vp) was determined using the adsorption branch of the N_2 isotherm curve at $P/P_0 = 0.98$ single point.

Scanning electron microscopy (SEM) images were obtained with a Philips Scanning Electron Microscope 505. The energy dispersive X-ray analysis (EDS) was performed using an EDAX DX PRIME 10 analyzer at a working potential of 15 kV

X-ray diffraction (XRD) was conducted using Cu Kα (λ = 0.154 nm) as a radiation source in an automatic Philips PW 1729 X-ray diffractometer. The samples were scanned from 5° to 60° (step size 0.02°; time per step 1.25 s). The average crystallite sizes (D) were estimated using the Scherrer equation [36]:

$$d = \frac{K\,\lambda}{\beta\,cos\theta} \tag{1}$$

where K is a constant equal to 0.9; λ the wavelength of the X-ray used; and β the effective linewidth (FWHM) of the observed X-ray reflection, obtained by curve-fitting procedure after Warren's correction for instrumental broadening and background subtraction.

Raman spectra were measured at room temperature in backscattering geometry with a Via Renishaw micro-Raman spectrometer equipped with an air-cooled CCD detector and edge filters. The emission line at 488.0 nm from an argon ion laser was focused on the sample under a Leica DLML microscope using 20× or 5× objectives. The power

of the incident beam was about 5 mW. Five 10 s accumulations were generally acquired for each sample. The resolution was 2 cm^{-1} and spectra were calibrated using the 520.5 cm^{-1} line of a silicon wafer. Spectra processing included baseline removal and curve fitting using a Gauss-Lorentz cross-product function by Peakfit 4.12 software (Systat Software Inc., San Jose, CA, USA, 2007).

Fourier Transform Infrared Spectroscopy (FTIR) was employed to characterize the prepared catalysts. The spectra were obtained in the 400–4000 cm^{-1} wavenumber range using KBr pellets in a Thermo Bruker IFS 66 FT-IR spectrometer.

The temperature programmed reduction (TPR) patterns were obtained in a flow system with a mixture of 10 vol.% H_2 and 90 vol.% N_2 (20 cm^3/min), by heating from room temperature up to 850 °C at 10 °C/min in a home-made equipment.

X-ray Photoelectron Spectroscopy (XPS) analysis was carried out in a *Multitecnic Specs* equipped with a dual Mg/Al X-ray source and a *PHOIBOS 150* hemispheric analyzer operating in the Fixed Analyzer Transmission (FAT) mode (30 eV). Spectra were recorded using Mg Kα radiation (1253.6 eV, 200 W) and pressure lower than 5.10^{-9} mbar during determination. The samples, gently pressed on the sample holder, were either evacuated for 10 min at 423 K or reduced in a flowing H_2/Ar (5%) mixture at 623 K for 10 min and then kept in ultra-high vacuum for at least 2 h before measurements. Binding energy values were referenced to C 1s at 284.6eV. Data analysis involved smoothing, non-linear Shirley-type background subtraction, curve fitting (mixed Gaussian–Lorentzian functions by a least-square method) and peak area determination by integration of the appropriate signal after data analysis (Esca Tools 4.2 software, Surface Interface Inc., Mountain View, CA). Surface composition was determined by the peak area ratios using the empirically derived atomic sensitivity factors reported by Wagner C. D [37].

2.4. Catalyst activity

The NO_3^-, NO_2^- and BrO_3^- reduction was carried out in a three-necked 100-mL Pyrex glass 100 mL semi-batch reactor equipped with a magnetic stirrer. In a typical run, 25, 50 or 100 mg of catalyst were employed. These catalysts were previously reduced in H_2 flow at 400 °C for 2 h, and then cooled in H_2 flow. After that, Ar was recirculated to remove H_2. Then, the catalyst was transferred to the reactor, which contained 50 mL of a degassed solution with 50 ppm of BrO_3^- or 100 ppm of NO_3^- or NO_2^-. The reaction was carried out at atmospheric pressure, at ambient temperature, and pure H_2, the reducing agent, was flowed during the reaction at 400 mL/min. Values of NO_3^-, NO_2^- or BrO_3^- conversion (X_{NO3^-}%) and selectivity to the detected products NO_2^- (S_{NO2^-}%), NH_4^+ (S_{NH4+}%), N_2 (S_{N2}%) or Br^-(S_{Br^-}%) after 180 min reaction were calculated for all the catalysts under study according to the following equations [38]:

$$X_{NO_3^-} = \frac{[NO_3^-]_{initial} - [NO_3^-]_t}{[NO_3^-]_{initial}} * 100\% \quad (2)$$

$$S_{NO_2^-} = \frac{[NO_2^-]_t}{[NO_3^-]_{initial} - [NO_3^-]_t} * 100\% \quad (3)$$

$$S_{NH_4^+} = \frac{[NH_4^+]_t}{[NO_3^-]_{initial} - [NO_3^-]_t} * 100\% \quad (4)$$

$$S_{N_2} = 100 - S_{NO_2^-}(\%) - S_{NH_4^+}(\%) \quad (5)$$

$$X_{BrO_3^-} = \frac{[BrO_3^-]_{initial} - [BrO_3^-]_t}{[BrO_3^-]_{initial}} * 100\% \quad (6)$$

$$S_{Br^-} = \frac{[Br^-]t}{[BrO_3^-]_{initial} - [BrO_3^-]_t} * 100\% \quad (7)$$

$$V_0 = \frac{[Ox]_{initial} - [Ox]_t}{[Ox]_t} \quad (8)$$

3. Results and discussion

3.1. Catalyst characterization

The morphological characterizations of the supports, performed by SEM, are shown in Fig. 1. Both supports prepared by the sol-gel method using NH_4OH as precipitant, exhibited a porous and uniform surface. The Zr/Ce atomic ratio on the 10ZrCe support was also determined by the EDS semi-quantitative analysis. A good agreement between theoretical Zr/Ce atomic ratio (0.19) and the obtained value (0.20) was found. This technique also allowed corroborating that the support contains 10 % of Zr (Table 1).

Table 1 presents the textural properties of the prepared supports. The specific surface area and the V_{pore} of CeO_2 and 10ZrCe supports are quite similar, like the morphology of the surfaces, analyzed by SEM. Besides, the addition of Zr noticeably decreases the pore diameter of CeO_2 which suggests that Zr^{4+} ions having smaller radius may agglomerate inside ceria pores [24,39].

Fig. 2 shows the isotherms obtained for all the prepared supports. In both cases, the isotherms were type IV, typical of mesoporous sample, such as oxide gels, industrial adsorbents or mesoporous molecular sieves. This type of isotherm indicates an initial monolayer-multilayer adsorption on the mesopore walls, followed by pore condensation. For pure ceria, the isotherm showed a hysteresis cycle type H2a, attributed to pore-blocking/percolation, or to cavitation-induced evaporation. The small step around $P/P_0 = 0.45$ could implied a cavitation process. On the other hand, for 10ZrCe support, the presence of hysteresis observed is assigned to capillary condensation. The hysteresis cycle is type H3, corresponding to non-rigid aggregates of plate-like particles [40]. It was found that the ZrO_2 addition improves the thermal stability of pure ceria, since it slows down the growth process of crystallites, thus preserving the specific surface [24].

From the obtained results, it can be inferred that the ceria-based materials synthesized in this work have adequate textural characteristics to be used as supports in the preparation of catalysts. The solids obtained by the simple sol-gel method used in this work are mesoporous and had a desirable specific surface which could favor that catalytic reaction reactions take place at the catalyst surface.

FT-IR spectra analysis of the supports and catalysts prepared are presented in Fig. 3. All FT-IR spectra show similar profiles. Relatively intense bands are observed near 3500, 1600 and 700 cm^{-1}. The first two correspond to (OH) stretching and deformation modes respectively, due to the hydrogen bonds of residual water molecules. Those below 700 cm^{-1} correspond to antisymmetric stretching modes of the Zr(Ce)-O bonds. According to the literature, residual water and OH^- groups can be detected according to the preparation method and calcination temperatures. At high frequencies (between 3400 and 2500 cm^{-1}), bands assigned to OH groups could also be observed. These bands are due to the fact that the Ce^{4+} is hydrolyzed with water or OH- molecules during the synthesis process, to give $[Ce(OH)_x(H_2O)_y]^{(4-x)+}$]. The number (x + y) corresponds to the Ce coordination number. Also, a band at 3510 cm^{-1} has been reported, assigned to a residual phase of cerium oxyhydroxide located within the pores [41,42].

The chemical properties and structural characteristics of Ce-Zr mixed oxides are strongly dependent on their atomic composition. In this sense, the XRD patterns of the supports and bimetallic catalysts are presented in Fig. 4. All the diffraction patterns show peaks at 2θ values of 28.5°, 33.1°, 47.5°, 56.3° and 59.1 corresponding to the reflections (111), (200), (220) and (311) of the fluorite-type cubic crystal structure of CeO_2 (PDF card 81−0792). The addition of Zr to the CeO_2 lattice did not produce appreciable modifications in the XRD patterns, (comparison between curves a) and b) indicating that a strong interaction at atomic/

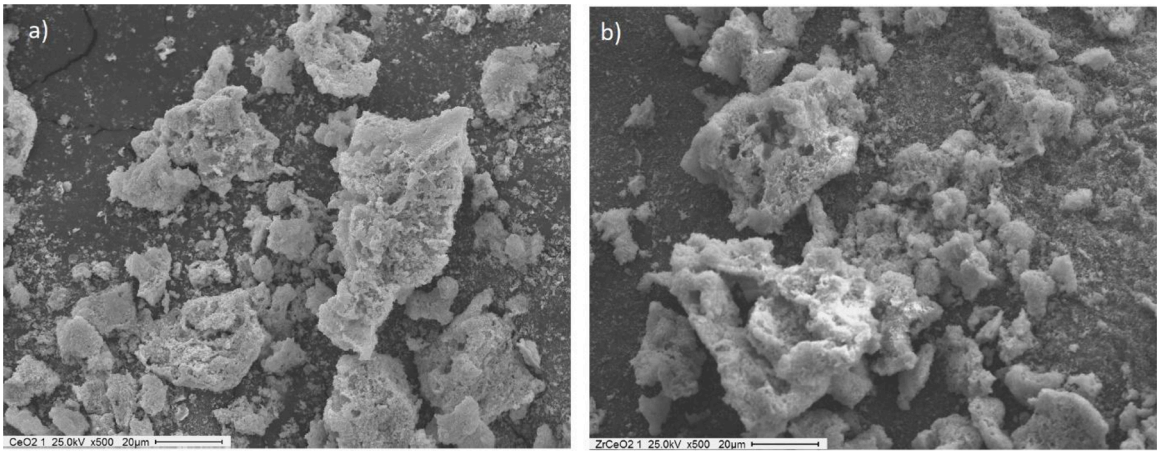

Fig. 1. SEM images of a) CeO_2, and b) $10ZrCeO_2$ support, both using 500X magnification.

Table 1
Textural properties and results of EDS for the prepared supports.

Catalyst	Specific area (m^2/g)	V_{pore} (cm^3/g)	D_{pore} (Å)	Theoretical Zr%	Experimental Zr%[a]	Theoretical Zr/Ce atomic ratio	Experimental Zr/Ce atomic ratio[a]
CeO_2	62	0.06	38	–	–	–	–
10ZrCe	66	0.07	44	0.19	0.20	10	11

a: determined by EDS.

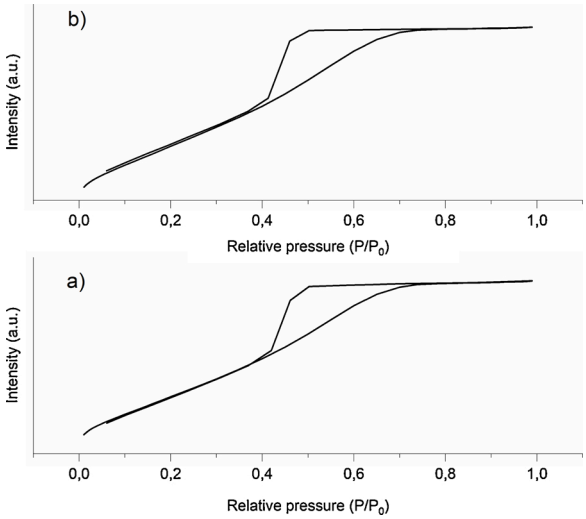

Fig. 2. N_2 adsorption/desorption isotherms at −196 ◦C for the prepared supports: a) CeO_2 and b) 10ZrCe.

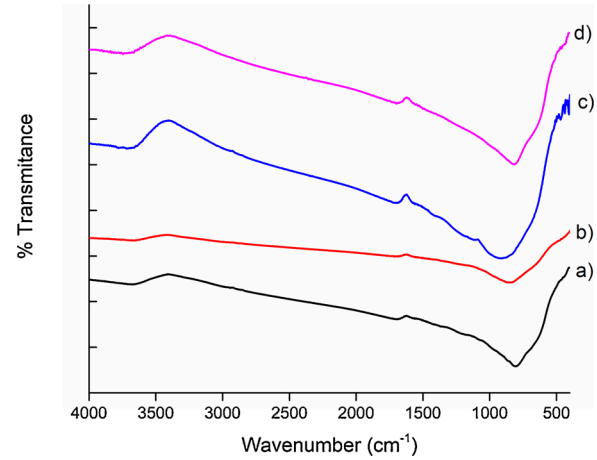

Fig. 3. FT-IR of the synthesized catalysts. a) CeO_2; b) $10ZrCeO_2$; c) PdCu/10ZrCe; d) PdCu/CeO_2.

molecular level between support and added species occurred with highly dispersed surface metal species. This would be an evidence of the Zr^{4+} incorporation in the CeO_2 lattice. [24,43].

No significant changes appeared in the patterns of the PdCu-containing catalysts. This indicates a well dispersion of the metals on the surface of the supports. Compared to CeO_2 mean crystals size calculated for CeO_2 (7.0 nm), 10ZrCe (6.7 nm) and the PdCu/10ZrCe (7.0 nm) samples, the little lower values found for the PdCu/CeO_2 sample indicate that the interaction between surface species and CeO_2 prevented coalescence of CeO_2 particles.

The Raman spectrum of the CeO_2 sample (Fig. 5A) exhibits a strong peak at about 460 cm^{-1}, attributed to the F_{2g} mode of the fluorite-like phase. This is in accordance with the XRD studies [44]. The weak bands at about 250, 595, and 1175 cm^{-1} are due to second-order transverse acoustic (2TA), defect-induced (D) mode, and second-order longitudinal optical (2LO) mode, respectively [45,46]. The F_{2g} mode is sensitive to grain size and to defects and/or distortion of the CeO_2 structure. Specifically: i) the F_{2g} band broadens and becomes asymmetric with a low frequency tail as the grain size decreases; ii) the presence of defects appears with new features at about 225 and 580 cm^{-1}, which are related to lattice defects introduced into the CeO_2 structure in order to maintain charge neutrality or to structure distortion due to incorporation of equivalent cations differing in size.

Comparing the Raman spectra of the CeO_2 and 10ZrCe supports it is apparent a slight shift to higher frequency and an increase of the tail in the lower frequency side as well as of the bands at about 250, 595, and 1175 cm^{-1}.These variations can be attributed to the incorporation of Zr^{4+}ions in the CeO_2 lattice: the difference in the ionic size of Ce^{4+}cation (0.097 nm) and Zr^{4+} (0.084 nm) promotes the lattice deformation as well as the presence of oxygen vacancies due to incorporation of Zr^{4+} ions. These results agree with the absence of zirconia reflections in the XRD pattern.

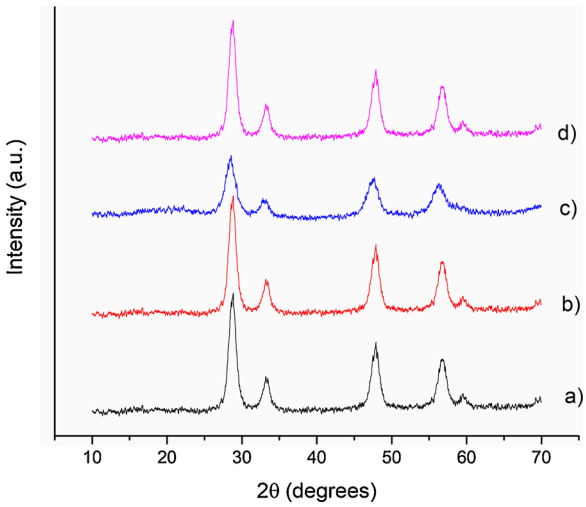

Fig. 4. XRD patterns of the CeO_2 –based catalysts. a) CeO_2; b)10ZrCe; c)PdCu/CeO_2; d)PdCu/10ZrCe.

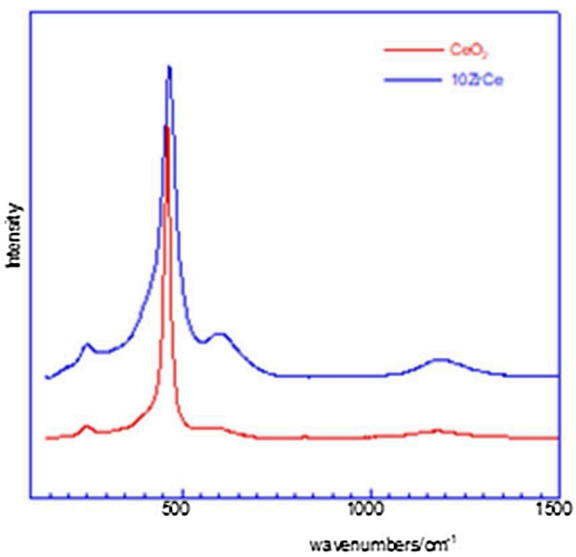

Fig. 5. Raman spectra of the CeO_2 and 10ZrCe supports.

Fig. 6 allows comparing the Raman spectra obtained for each support with the addition of PdCu. Fig. 6A compares the pure CeO_2 support with the PdCu/CeO_2 catalyst, and Fig. 6B compares 10ZrCe with PdCu/10ZrCe catalyst. In both cases, the addition of the metal and the promoter to the support causes an increase of the tail in the lower frequency side due to a lowering of the Ce–O bond and an increase in intensity of the bands at about 250, 595, and 1175 cm^{-1}. The increase in intensity of the band at about 595 cm^{-1}, which encloses contributions due to oxygen vacancies and defects due to changes in cations coordination, shown by the addition of PdCu to the CeO_2 lattice can be attributed to the strong interaction between the supported species and the support [44,47].

XPS analysis allowed determining the chemical composition of the catalytic surface and the nature of interactions between the supported metallic species and CeO_2. The BE values obtained from curve fitting procedures of the various regions are collected in Table 2.

Figure S1 illustrates the Ce*3d*, O*1 s* and C*1 s* regions collected on CeO_2. The fraction of Ce^{3+}species was calculated by the ratio $Ce^{+3}/(Ce^{+3}+Ce^{+4})$ [48], that is the area of Ce^{+3} signals to the total Ce*3d* $[Ce^{+3}/(Ce^{+3}+Ce^{+4})$ signals, obtained by curve fitting procedures. This value resulted 11 % of the total components.

The O1 s binding energy (BE) for CeO_2 normally can vary between 529.6 eV and 530.3 eV, corresponding to Ce^{4+}– O and Ce^{3+}– O bonds, respectively. Surface OH groups are expected to contribute with a component at a BE of 531.6 eV. The O*1 s* region (Figure S1A) was resolved with a main component at 529.4 eV and two weaker peaks at 531.1 and 532.7 eV, ascribed to lattice oxygen (Ce-O bond), surface oxygen species, and hydroxyl groups, respectively. The major peaks at around 529.2 and 531.3 eV are characteristic of lattice oxygen (O_{latt}) and surface adsorbed oxygen (O_{sur}), respectively [49]. It was demonstrated previously in literature that the concentration of Ce^{+3} is related to the level of oxygen vacancy [50]. The presence of Ce^{+3}, Ce^{+4} and O_{latt} indicates the presence of oxygen vacancies on the support.

Figure S2 shows the profiles and fitting for the 10ZrCe support. The Ce*3d* profile (Figure S2C) was very similar to that recorded for pure CeO_2 corresponding to Ce^{4+} species and Ce^{3+} with Ce$3d_{5/2}$ main component having BE of 882.8 eV (v) and 885.5 eV (v'), respectively. The fraction of Ce^{3+} species, calculated by ratio $Ce^{3+}/(Ce^{3+} + Ce^{4+})$, resulted slightly higher than 12 % in comparison with CeO_2 support. This may indicate a higher formation of oxygen vacancies in the 10ZrCe support, and it is in accordance with the Raman analysis. The O_{1s} peak (Figure S2A) resulted as the convolution of components at 529.3, 530.5 and 532.1 eV. The components at 529.3 and 532.1 eV are in close agreement with those of CeO_2, whereas the component at 530.5 could arise from oxygen contribution of surface ZrO_2 [51]. Figures S2D and S2E shows the XPS results for Zr$3d_{5/2}$ at 182.2 eV and Zr$3p_{3/2}$ at 332.8 eV. Both are in agreement with the values reported in the literature for

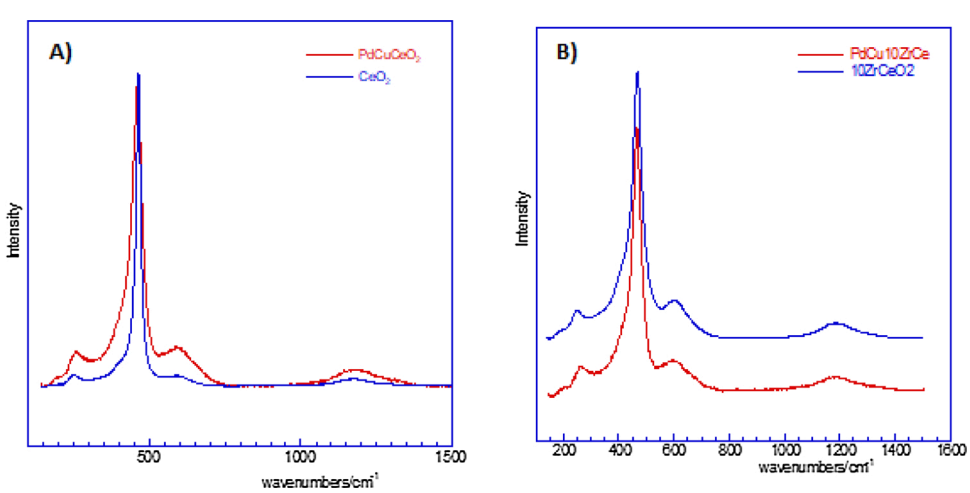

Fig. 6. Raman spectra of CeO_2 and PdCu/CeO_2 (A), and 10ZrCe and PdCu/10ZrCe (B).

Table 2
BE values obtained by curve fitting of the most representative regions of the various elements.

Catalyst	O1 s BE(eV)	Ce3d BE(eV)	$Zr3d_{5/2}$ BE(eV)	$Zr3p_{3/2}$ BE(eV)	$Pd3d_{5/2}$ BE(eV)
CeO_2	529.4 531.1 532.7	Ce(IV): 882.6, 888.6, 898.5, 901.1, 907.4, 917.2; Ce(III): 885.5, 903.8	——	——	——
10ZrCe	529.6 530.5 532.1	Ce(IV): 882.8, 889.3, 898.7, 901.3, 907.5, 917.1; Ce(III): 885.5, 903.5	182.1	332.9	—
$PdCu/CeO_2$	529.4 530.5 532.5	Ce(IV): 882.7, 888.8, 898.6, 901.3, 907.5, 917.1; Ce(III) 885.03, 903.4;	——	—	337.9
$PdCu/10ZrO_2Ce$	529.5 530.8 532.5	Ce(IV): 882.6, 888.7, 898.7, 900.9, 906.6, 916.9. Ce(III): 881.1, 884.9, 897.5, 903.4	182.2	332.9	337.2

ZrO_2 [52].

For $PdCu/CeO_2$ catalyst, the XPS peaks of Ce*3d*, O*1 s* and Pd*3d* are illustrated in Figure S3. The region corresponding to Cu*2p* was not recorded due to the low resolution of the XPS equipment employed. If compared to CeO_2, the addition of Pd and Cu species did not affect the Ce*3d* profile (Figure S3B), both in the BE values and $Ce^{3+}/(Ce^{3+} + Ce^{4+})$ ratio. The curve fitting procedure gave Ce$3d_{5/2}$ main component with BE of 882.7 eV (v) and 885.0 eV (v') corresponding to Ce^{4+} and Ce^{3+} species, respectively. The fraction of Ce^{3+} species, resulted 11 %, in full agreement with the value determined for CeO_2. For Pd, has the Pd$3d_{5/2}$ peak at 336.6 eV with a doublet separation (Pd$3d_{5/2}$-Pd$3d_{3/2}$) of 5.31 eV. In the form of metal particles, the $Pd3d_{5/2}$ has a BE equal to 335.8 eV [53–55]. The presence of Pd sites allows H_2 dissociation, and consequently, the NO_3^- reduction. For the catalyst $PdCu/CeO_2$, the $Pd3d_{5/2}$ component (Figure S3C) displayed a BE value of 337.8 eV, 1.2 eV higher than that recorded for PdO. This shift indicates the presence of PdO species dispersed and interacting with the ceria surface [49,56]. The O*1 s* peak deconvolution resulted in three components at 529.3, 530.5 and 532.1 eV (Figure S3A). The components at 529.3 and 532.1 eV are in close agreement with those of CeO_2, whereas the component at 530.5 eV could arise from oxygen contribution of surface PdO [53–55]. The proximity of Pd° and PdO would favor the catalytic reduction of the oxyanions, since H_2 can be dissociated on the Pd° sites, which then are oxidized to PdO [56].

In the case of PdCu/10ZrCe catalyst, the representative XPS regions corresponding to Ce*3d*, O*1 s*, Zr*3d* and Zr*3p*+Pd*3d* are illustrated in Figure S4. As explained before, the region corresponding to Cu*2p* was not recorded. In comparison to the 10ZrCe system, the addition of Pd and Cu-species affected the Ce*3d* profile (Figure S4B), both in the BE values and in the $Ce^{3+}/(Ce^{3+} + Ce^{4+})$ ratio. The curve fitting procedure gave for Ce$3d_{5/2}$ a main component with BE of 882.7 eV (v) and related peaks corresponding to Ce^{4+} and components with BE of 881.2 (u°) and 885.0 eV (v') assigned to Ce^{3+} species. The fraction of Ce^{3+} species, resulted 27 %, indicative of an increase in the formation of this species. The high value of the Ce^{3+} fraction could be originated from the strong interaction between surface species and support. The Ce^{3+} content was increased by loading Pd species. In this sense, the PdCu/10ZrCe surface had more oxygen vacancies than $PdCu/CeO_2$. The increase of Ce^{3+} content favors the catalytic activity, since allows a greater chemisorption of H_2 on the catalytic surface, and consequently, a better oxyanions removal. As the Cu*2p* region was not recorded, the effect of the CuO addition cannot be ascertained.

The O*1 s* peak resulted as the convolution of components at 529.3, 530.5 and 532.1 eV (Figure S4A). The components at 529.3 and 532.1 eV are in close agreement with those of 10ZrCe, whereas the component at 530.5 could arise from oxygen contribution of surface species such as PdO and ZrO_2. The Zr$3d_{5/2}$ peak exhibited a BE of 182.2 eV (Figure S4C), as for the unsupported ZrO_2 oxide. For Pd-containing compounds in the presence of ZrO_2, there is generally an overlapping between the Zr*3p* and Pd*3d* regions; the Pd$3d_{5/2}$-Pd$3d_{3/2}$ energy splitting is 5.3 eV, whereas that of the Zr*3p* doublet is 13.6 eV [56,57]. As shown in Figure S4D, the overlapping of the Pd*3d* and Zr*3p* regions was resolved by curve fitting resulting in a Zr$3p_{3/2}$ component having a BE of 332.8 eV as for ZrO_2, and Pd$3d_{5/2}$ peak with BE of 337.8 eV due to PdO. The value obtained for the supported Pd species is shifted by 1.2 eV with respect to the value of bulk PdO but unchanged with respect to the value obtained for the CeO_2 support. The presence of Pd° would provide more sites for H_2 dissociation, which makes the reaction to proceed more rapidly [56].

In the NO_3^- reduction, it was demonstrated that the support plays a key role. The electronic interaction between Pd particles and the support has influence in the catalytic performance [58]. The XPS data obtained in this work provide evidence that the Pd metal sites are present on both prepared supports. Surface composition, expressed as atomic ratios, yielded a Pd/Ce atomic ratio of 0.023 for $PdCu/CeO_2$, and a Pd/(Zr + Ce) atomic ratio equal to 0.017 for $PdCu/10ZrCeO_2$ catalyst.

For the $PdCu/CeO_2$ catalyst, according to sample composition (1%Pd and 99 % CeO_2), a bulk atomic ratio Pd/Ce equal to 0.016 was calculated; for the PdCu/10ZrCe [1%Pd /(10 % ZrO_2+ 90 % CeO_2)], a bulk atomic ratio Pd/Ce + Zr equal to 0.015 was expected.

Comparing surface and bulk composition, the $PdCu/CeO_2$ sample shows an enrichment of Pd surface species.

TPR results are presented in Fig. 7. In this figure, all the reduction peaks appear at less than 650 °C, and can be attributed to surface Ce species. According to the literature, ZrO_2-CeO_2 mixed oxides present two representative reduction peaks at the TPR profile: the first one located from 280 to 600 °C corresponds to the reduction of the outer layers of Ce^{4+} to Ce^{3+}. A second peak from 650 to 850 °C can be assigned to the reduction of the inner layer Ce^{4+} and also bulk oxygen. In the 10ZrCe support, the peak at 600 °C, is attributed to the reduction of surface Ce species [22,59].

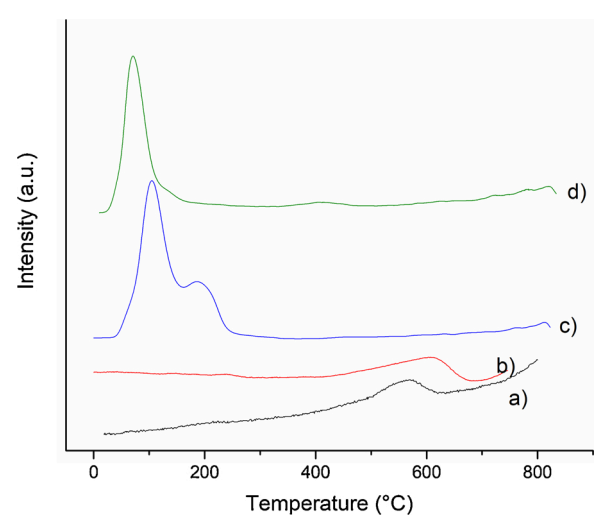

Fig. 7. TPR results for the prepared catalysts. a)CeO_2; b)10ZrCe; c)$PdCu/CeO_2$; d)PdCu/10ZrCe.

In the TPR profiles of the Pd catalysts, it is possible to distinguish a large peak centred around 150 °C, assigned to the reduction of PdO to Pd°. In the PdCu/10ZrCe catalyst, this peak also appeared, and is shifted to lower temperatures [60,61]. When Zr is added to the ceria support, it can be observed that the reduction temperature of the peak corresponding to Pd, decreases. This is due to more oxygen vacancies are generated by the Ce^{4+}/Ce^{3+} pair, as observed in Raman analysis.

In the $PdCu/CeO_2$ catalyst, a second peak extended around 200 °C is observed. This peak corresponds to the reduction of CuO to Cu°, and is absent in the catalyst PdCu/10ZrCe. In this catalyst, the presence of Pd and Ce^{3+}/Ce^{4+} favors the spillover of H_2, so the Cu oxides can be reduced at lower temperature, in comparison to the necessary temperature in a monometallic Cu catalyst (300−400 °C) [62,63]. For PdCu/10ZrCe catalyst two Cu reduction steps are observed. A small peak, which was extended between 300 and 400 °C, corresponds to the reduction of CuO to Cu° and the reduction of copper oxides promoted by the presence of the noble metal Pd are observed.

3.2. Catalytic activity

Some blank reactions, before the catalytic test, were performed. In the first blank test, H_2 was bubbled in an aqueous solution containing 100 ppm NO_3^-, 100 ppm NO_2^- or 50 ppm solution of BrO_3^- in the absence of catalyst. The second test was performed under these same conditions in the presence of the support. In both cases, it was found that NO_3^-, NO_2^- and BrO_3^- removal were null.

The results of elimination of the oxyanions of interest (X%), including the selectivity (S%) towards the different products and the initial rate (V_0), employing the prepared catalyst, are presented in Table 3. The elimination curves of the different oxyanions are presented in Fig. 8.

The results in Table 3 indicate that the monometallic catalysts are active in the elimination of the oxyanions and higher elimination was achieved using bimetallic instead of monometallic catalysts. All the PdCu-containing catalysts were active in the elimination of the oxyanions of interest. Contrary to what is reported in the literature, Pd monometallic catalysts supported on cerium materials are active in the elimination of NO_3^-. When Al_2O_3 or SiO_2 are used as support, Pd catalysts are inactive in NO_3^- elimination [64]. In the catalyst used in this work, NO_3^- and NO_2^- are mainly reduced to N_2 and the presence of small amounts of NH_4^+ (an undesirable product) was observed, with selectivity minor to 1% in almost every case. It was also observed that the NO_3^- elimination generates NO_2^- as intermediate, which disappears at the end of the reaction. In the elimination of NO_3- and NO_2-, catalysts containing only Cu exhibit a lower conversion compared to those containing Pd and Cu. According to the generally accepted mechanism for this reaction, the promoter metal (Cu, in this case) takes an oxygen atom from NO_3^- and in a second step, the noble metal (Pd) dissociates the H_2 to atomic H, which reduces the promoter metal, Cu. [52,65,66]. The presence of Pd (corroborated by XPS) and Cu in zero valent state is necessary for a good elimination of the oxyanions, both for the activation of the N═O bonds, and for the hydrogen chemisorption and spillover [33]. The TPR results also determined the interaction between Cu and Pd, since Cu could be reduced at lower temperatures than usual. Furthermore, as seen by XPS, CeO_2 is an oxide susceptible of being reduced, which can interact with metal Pd, leading to electron transfer from the noble metal to CeO_2, favoring the oxyanion elimination. Both catalysts prepared in this work exhibited great selectivities towards N_2: 98.71 % for $PdCu/CeO_2$ and 99.93 % for PdCu/10ZrCe. The catalyst PdCu/10ZrCe presented the higher reaction rate, in comparison with $PdCu/CeO_2$, as was shown in Table 3. This difference is more notorious in the NO_3^- reduction.

In the same way for NO_3^- and NO_2^- reduction, the generally accepted mechanism for BrO_3^- reduction is their adsorption on the catalyst, followed by dissociative H_2 adsorption, and finally the reduction step [67,68]. According to the results presented in Table 3 it can be observed that BrO_3^- is reduced exclusively to Br- in all cases. Both PdCu-catalysts were active in BrO_3^- removal, even more than those that only containing Pd o Cu separately. The difference can be attributed to the H_2 chemisorption on metals. Considering the classification of bond, the H_2 chemisorption is weak for Cu, and moderate for Pd [67,69]. This would explain the greater activity of Pd/CeO_2 and Pd/10ZrCe catalysts in comparison with Cu/CeO_2 and Cu/10ZrCe. The highest removal percentages were found for PdCu-containing catalyst: 50 % y 75 % for $PdCu/CeO_2$ and PdCu/10ZrCe, respectively. The presence of more oxygen vacancies in the 10ZrCe support in comparison with the pure ceria, evidently improves the catalytic performance. On the other hand, the initial reaction rate is lower for BrO_3^- reduction, when compared to NO_3^- and NO_2^- reduction. The difference may be due to the strong dependence of BrO_3^- adsorption and reduction with pH. The redox potential of BrO_3^-/Br^- decreases with increasing pH, and for high pH solution, the reducibility of BrO_3^- would be inhibited [63,68,70].

In these catalysts, the noble metal, Pd, has the function of activate the H_2, allowing the reduction of the different oxyanions$^-$. During the reduction process, the support is found in a reduced state (Ce^{3+}). This reduction of Ce^{4+} to Ce^{3+} generates oxygen vacancies, first at the metal-support interface, then progressively into the bulk. Thus, the reduction of the anions can occur by the interaction of oxygen atoms of NO_3^-, NO_2^- or BrO_3^- with the oxygen vacancies created on the support (Fig. 9). Therefore, the oxygen vacancies that exist in the CeO_2 and 10ZrCe redox supports, as well as their interaction with the Pd, as observed by XPS, make the resulting system active in the oxyanions hydrogenation [71]. The high specific surface and well dispersion of the metal particles in the surface of the supports also contributes to the catalytic performance.

The results shown in Table 3 reveal that PdCu/10ZrCe catalyst has the best catalytic performance. The elimination of NO_3^- and NO_2^- was complete being more active in the elimination of BrO_3^- compared to $PdCu/CeO_2$ (75 % vs. 50 %). Besides, PdCu/10ZrCe has the best selectivity towards the products of interest N_2 and Br^- (>99.9 % in every case). This can be attributed to the addition of ZrO_2 to CeO_2 that increases the oxygen vacancies of CeO_2. The vacancies would allow increasing the interaction between the support and the oxyanions present in water. This is due to the partial replacement of Ce^{4+} with Zr^{4+} in the ceria structure, as was seen by XRD, XPS and Raman spectroscopy.

The PdCu/10ZrCe catalyst was also evaluated using groundwater extracted from the Puelche Aquifer in order this catalyst has a practical application (Fig. 8). The Puelche Aquifer has low salinity

Table 3
Elimination of NO_3^-, NO_2^- y BrO_3^-, oxyanion initial conversion rate values, and product selectivities using the prepared catalysts (atmospheric pressure, 180 min).

Catalyst	NO_2^- elimination				NO_3^- elimination					BrO_3^- elimination		
	V_0*	$\%X_{NO2-}$	$\%S_{NH4+}$	$\%S_{N2}$	V_0*	$\%X_{NO3-}$	$\%S_{NO2-}$	$\%S_{NH4+}$	$\%S_{N2}$	V_0*	$\%X_{BrO3-}$	$\%S_{Br-}$
Cu/CeO_2	–	–	–	–	–	–	–	–	–	–	5	100
Pd/CeO_2		65	0.09	99.91		12	1.8	0.08	98.14		23	100
$PdCu/CeO_2$	3.3	100	0.05	99.65	3.2	100	1.2	0.09	98.71	0.40	50	100
Cu/10ZrCe	–	–	–	–	–	–	–	–	–		21	100
Pd/10ZrCe		81	1.4	98.6		25	0.5	0.03	99.2		36	100
PdCu/10ZrCe	5	100	0.06	99.94	5.6	100	–	0.07	99.93	0.93	75	100

* Initial rate at 15 min V_0: NO_3^-consupmtion (ppm)/min.

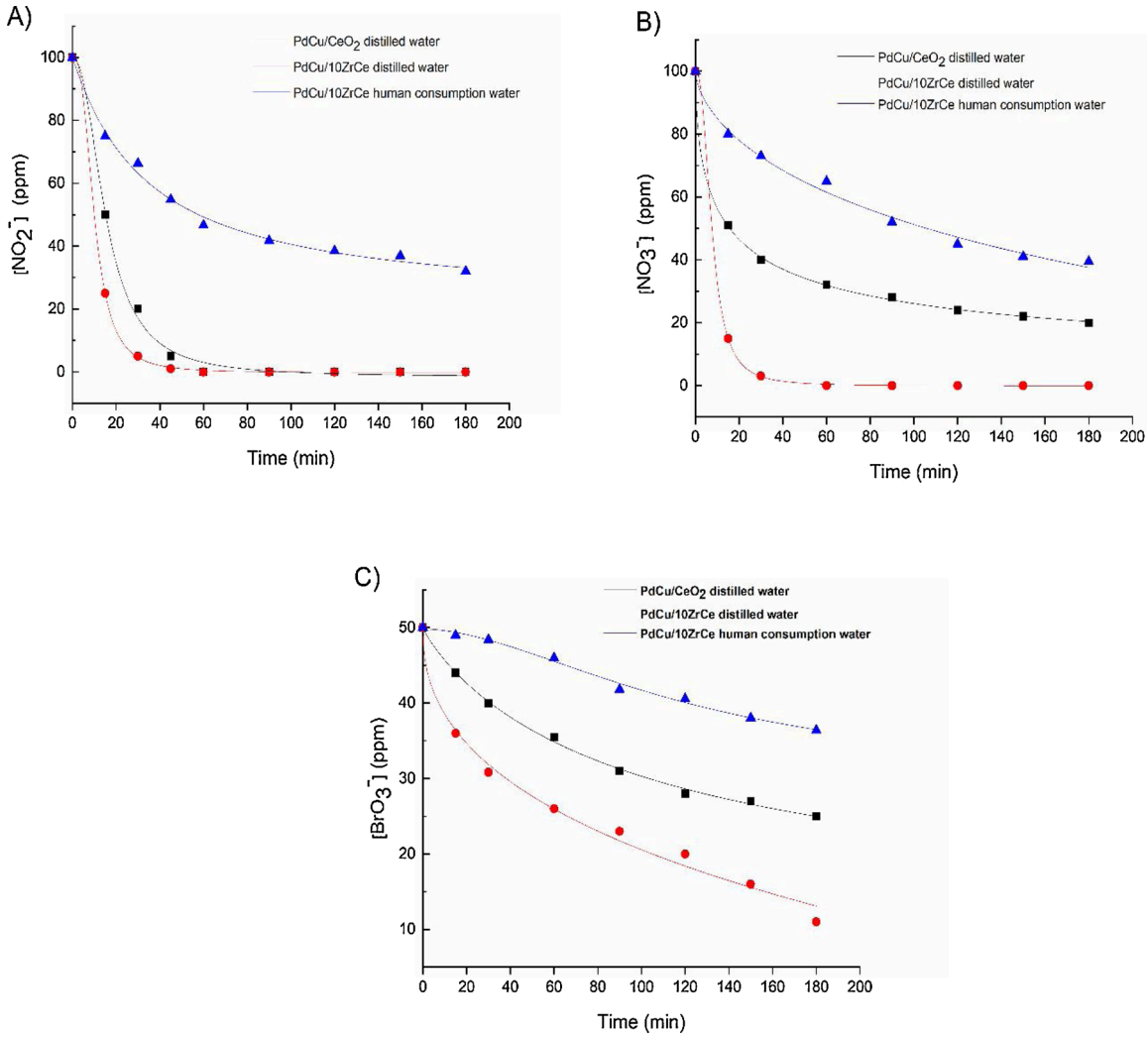

Fig. 8. Oxyanions concentration versus time for (A) NO_2^-, (B) NO_3^-, and (C) BrO_3^- in distilled and groundwater.

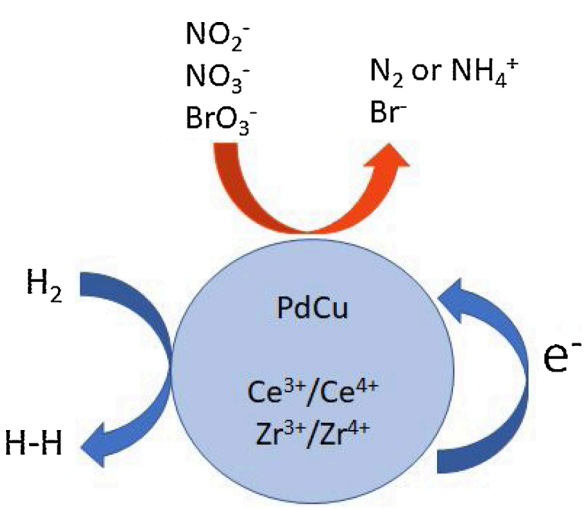

Fig. 9. NO_3^-, NO_2^- y BrO_3^- reduction, over the PdCu/10ZrCe surface.

(approximately 585 mg/L), being sodium bicarbonate the most abundant anion present and Its potability is only affected by the NO_3^- content, especially in urbanized areas [2,10]. Although the PdCu/10ZrCe catalyst was active in the elimination of all the studied anions studied (% X_{NO3-} = 60 %, X_{NO2-} = 70 %, X_{BrO3-} = 27 %), a slowdown during the reaction was observed. This is probably due to the masking of the active phase by the different ions present in the real water samples, especially due to the abundant presence of bicarbonate ions present. It is well-established that bicarbonate ions present similar chemical properties to NO_3^-, and thus it can be expected that both anions would be adsorbed on the same catalytic sites. The selectivities in this water sample to the products of interest were >98 % for N_2 in the NO_3^- and NO_2^- elimination and 100 % for BrO_3^- removal.

4. Conclusions

PdCu catalysts were prepared on supports based on pure CeO_2 and also adding ZrO_2. These supports were synthesized by a simple sol-gel method using NH_4OH as the precipitating agent. This method allowed obtaining mesoporous materials containing oxygen vacancies. The addition of Zr^{4+} ions in the CeO_2 lattice increases the oxygen vacancies on the 10ZrCe support.

The prepared catalysts were active in the elimination of the anions NO_3^-, NO_2^- and BrO_3^-, with high conversion and selectivity percentages towards the products of interest (Br^- and N_2). The PdCu/10ZrCe catalyst was the most active and selective, demonstrating the high promoter effect of the CeO_2-ZrO_2 support on the reaction studied. In the catalyst reduction with H_2, Ce^{4+} is reduced to Ce^{3+}, generating oxygen vacancies at the metal-support interface. The reduction occurs by interaction of

their oxygen atoms with these oxygen-vacant sites generated. In the PdCu/10ZrCe catalyst, it is observed that not only does the reduction capacity increase even more compared to the same catalyst supported on pure CeO_2, but also the selectivity. The addition of Zr on the ceria enhances the ability of the last support to activate NO_3^- and reduce them to N_2.

Funding

The authors would like to thank the following institutions for funding this work: CONICET (PIP 1178), UNLP (Project X633 and X802) and ANPCyT (PICT 2016/1391). We also thank ANPCyT for the purchase of the SPECS multitechnique analysis instrument (PME8-2003).

CRediT authorship contribution statement

Marisa B. Navas: Investigation, Writing - original draft, Visualization. **Hernán P. Bideberrripe:** Investigation, Resources. **Carmen I. Cabello:** Supervision. **Delia Gazzoli:** Investigation, Resources, Writing - original draft. **Mónica L. Casella:** Supervision, Funding acquisition. **María A. Jaworski:** Conceptualization, Investigation, Resources, Writing - original draft.

Declaration of Competing Interest

The authors declare that they have no known competing financial interests or personal relationships that could have appeared to influence the work reported in this paper.

Acknowledgment

We are grateful to Ms. Mariela Theiller for her technical support with SEM analysis.

Appendix A. Supplementary data

Supplementary material related to this article can be found, in the online version, at doi:https://doi.org/10.1016/j.cattod.2020.08.012.

References

[1] J. Xu, Y. Pu, W. Qi, X. Yang, Y. Tang, P. Wan, A. Fisher, Chemical removal of nitrate from water by aluminum-iron alloys, Chemosphere 166 (2017) 197–202, https://doi.org/10.1016/j.chemosphere.2016.09.102.
[2] M. Zabala, S. Martínez, M. Manzano, L. Vives, Groundwater chemical baseline values to assess the Recovery Plan in the Matanza-Riachuelo Riverbasin, Argentina, Sci. Total Environ. 541 (2016) 1516–1530, https://doi.org/10.1016/j.scitotenv.2015.10.006.
[3] Y. Zhao, N. Rao, L. Lefferts, Adsorbed species on Pd catalyst during nitrite hydrogenationapproaching complete conversion, J. Catal. 337 (2016) 102–110, https://doi.org/10.1016/j.jcat.2016.02.007.
[4] Y. Zhai, X. Zhao, Y. Teng, X. Li, J. Zhang, J. Wu, R. Zuo, Groundwater nitrate pollution and human health risk assessment by using HHRA model in an agricultural area, Ecotoxicol. Environ. Saf. 137 (2017) 130–142, https://doi.org/10.1016/j.ecoenv.2016.11.010.
[5] Faridullah, N. Malik, I. Fareed, M. Irshad, Reducing the leachability of nitrate phosphorous and heavy metals from soil using waste material, Braz. J. Chem. Eng. 34 (03) (2017) 715–726, https://doi.org/10.1590/0104-6632.20170343s20150617.
[6] S. Citak, S. Sonmez, Effects of conventional and organic fertilization on spinach (*Spinacea oleracea* L.) growth, yield, vitamin C and nitrate concentration during two successive seasons, Sci. Hortic. 126 (2010) 415–420, https://doi.org/10.1016/j.scienta.2010.08.010.
[7] USEPA Regulated Drinking Water Contaminants: Inorganic Chemicals. Accessed on 19/02/2020. Available online: https://www.epa.gov/ground-water-and-drinking-water/national-primary-drinking-water-regulations.
[8] Nitrate and Nitrite in Drinking-water. Background Document for Development of WHO Guidelines for Drinking-water Quality, World Health Organization, 2011. Accessed on 19/02/2020. Available online: https://www.who.int/water_sanitation_health/dwq/chemicals/nitratenitrite2ndadd.pdf.
[9] ANMAT Argentina Available online Accessed on 19/02/2020. http://www.anmat.gov.ar/alimentos/codigoa/CAPITULO_XII.pdf.
[10] S. Armengol, M. Manzano, S. Bea, S. Martínez, Identifying and quantifying geochemical and mixing processes in the Matanza-Riachuelo Aquifer System, Argentina, Sci. Total Environ. 599–600 (2017) 1417–1432, https://doi.org/10.1016/j.scitotenv.2017.05.046.
[11] L. Dongmei, W. Zhiwei, Z. Qi, C. Fuyi, S. Yujuan, L. Xiaodong, Drinking water toxicity study of the environmental contaminant—Bromate, Regul. Toxicol. Pharmacol. 73 (2015) 802–810, https://doi.org/10.1016/j.yrtph.2015.10.015.
[12] F. Soltermann, C. Abegglen, M. Tschui, S. Stahel, U. Von Gunten, Options and limitations for bromate control during ozonization of wastewater, Water Res. 116 (2017) 76–85, https://doi.org/10.1016/j.watres.2017.02.026.
[13] J. Wang, L. Chu, Biological nitrate removal from water and wastewater by solid-phase denitrification process, Biotechnol. Adv. 34 (6) (2016) 1103–1112, https://doi.org/10.1016/j.biotechadv.2016.07.001.
[14] J. Martínez, A. Ortíz, I. Ortíz, State-of-the-art and perspectives of the catalytic and electrocatalytic reduction of aqueous nitrates, Appl. Catal. B 207 (2017) 42–59, https://doi.org/10.1016/j.apcatb.2017.02.016.
[15] T. Strathmann, C. Werth, J. Shapley, Chapter 22 - Heterogeneous Catalytic Reduction for Water Purification: Nanoscale Effects on Catalytic Activity, Selectivity, and Sustainability. Author Links Open Overlay Panel. Nanotechnology Applications for Clean Water (Second Edition), Solutions for Improving Water Quality. Micro and Nano Technologies, 2014, pp. 339–349.
[16] Y. Kim, M. Kim, M. Choi, Synergistic integration of catalysis and ion-exchange for highly selective reduction of nitrate into N2, Chem. Eng. J. 289 (2016) 423–432, https://doi.org/10.1016/j.cej.2016.01.002.
[17] F. Zoppas, F. Marchesini, A. Devard, A. Bernardes, E. Miró, Controlled deposition of Pd and in on carbon fibers by sequential electroless plating for the catalytic reduction of nitrate in water, Cat. Commun. 78 (2016) 59–63, https://doi.org/10.1016/j.jece.2018.07.015.
[18] Q. Yang, F. Yao, Y. Zhong, D. Wang, F. Chen, J. Sun, S. Hua, S. Li, X. Li, G. Zeng, Catalytic and electrocatalytic reduction of perchlorate in water – a review, Chem. Eng. J. 306 (2016) 1081–1091, https://doi.org/10.1016/j.cej.2016.08.041.
[19] Q. Xiao, S. Yu, L. Li, T. Wang, X. Liao, Y. Ye, An overview of advanced reduction processes for bromate removal from drinking water: reducing agents, activation methods, applications and mechanisms, J. Hazard. Mater. 324 (B) (2017) 230–240, https://doi.org/10.1016/j.jhazmat.2016.10.053.
[20] F. Ruiz-Beviá, M. Fernández-Torres, Effective catalytic removal of nitrates from drinking water: an unresolved problem? J. Clean. Prod. 217 (2019) 398–408, https://doi.org/10.1016/j.jclepro.2019.01.261.
[21] J. Sun, J. Zhang, H. Fu, H. Wan, Y. Wan, X. Qu, D. Yin, S. Zheng, Enhanced catalytic hydrogenation reduction of bromate on Pd catalyst supported on CeO_2 modified SBA-15 prepared by strong electrostatic adsorption, Appl. Catal. B 229 (2018) 32–40, https://doi.org/10.1016/j.apcatb.2018.02.009.
[22] H. Zhang, W. Hu, C. Zhou, H. Liu, P. Yao, J. Wang, Y. Chen, A new understanding of CeO_2-ZrO_2catalysts calcinated at different temperatures: Reduction property and soot-O_2 reaction, Appl. Catal. A Gen. 563 (2018) 204–215, https://doi.org/10.1016/j.apcata.2018.07.012.
[23] D. Nakonieczny, M. Antonowicz, Z. Paszendaa, T. Radko, S. Drewniak, W. Bogaczd, C. Krawczyke, Experimental investigation of particle size distribution and morphology of alumina-yttria-ceria-zirconia powders obtained via sol–gel route, Biocybern. Biomed. Eng. 38 (2018) 535–543, https://doi.org/10.1016/j.bbe.2018.02.010.
[24] K. Aribi, Z. Soltani, M. Ghelamallah, P. Granger, Structure, morphology and reducibility of ceria-doped zirconia, J. Mol. Struct. 1156 (2018) 369–376, https://doi.org/10.1016/j.molstruc.2017.11.104.
[25] D. Gerçeker, I. Onal, A DFT study on CO oxidation on Pd_4 and Rh_4clusters and adsorbed Pd and Rh atoms on CeO_2 and $Ce_{0.75}Zr_{0.25}O_2$ supports for TWC applications, Appl. Surf. Sci. 285B (2013) 927–936, https://doi.org/10.1021/acs.jpcc.5b09293.
[26] J. Kasper, P. Fornasiero, M. Graziani, Use of CeO2-based oxides in the three-way catalysis, Catal. Today 50 (2) (1999) 285–298.
[27] A. Bueno-López, K. Krishna, M. Makkee, J. Moulijn, Enhanced soot oxidation by lattice oxygen via La^{3+}-doped CeO2, J. Catal. 230 (2005) 237–248, https://doi.org/10.1016/j.jcat.2004.11.027.
[28] W. Hernandez, O. Laguna, M. Centeno, J. Odriozola, Structural and catalytic properties of lanthanide (La, Eu, Gd) doped ceria, J. Solid State Chem. 184 (2011) 3014–3020, https://doi.org/10.1016/j.jssc.2011.09.018.
[29] K. Polychronopoulou, F. Zedan Katsiotis, M. Baker, A. AlKhooriSiham, Y. AlQaradawi, S. HinderSaeedAlHassan, Rapid microwaveassisted sol-gel synthesis of CeO2and CexSm1-xO2nanoparticle catalystsfor CO oxidation, J. Mol. Catal. A Chem. (2016), https://doi.org/10.1016/j.molcata.2016.11.039.
[30] D. Terribile, A. Trovarelli, J. Llorca, C. de Leitenburg, G. Dolcetti, The preparation of high surface area CeO_2-ZrO_2 mixed oxides by a surfactant-assisted approach, Catal. Today 43 (1998) 79–88, https://doi.org/10.1016/S0920-5861(98)00136-9.
[31] M. Dumont, E. Nunes, W. Vasconcelos, Use of a design of experiments approach for preparing ceria–zirconia–alumina samples by sol–gel process, Ceram. Int. 42 (2016) 9488–9495, https://doi.org/10.1016/j.ceramint.2016.03.021.
[32] K. Resende, C. Teles, G. Jacobs, B. Davis, D. Cronauer, A. Kropf, C. Marshall, C. Hori, F. Noronha, Hydrodeoxygenation of phenol over zirconia supported Pd bimetallic catalysts. The effect of second metal on catalyst performance, Appl. Catal. B 232 (2018) 213–231, https://doi.org/10.1016/j.apcatb.2018.03.041.
[33] M. Kim, D. Lee, S. Chung, T. Kim, H. Cho, Y. Lee, Pd–Cu bimetallic catalysts supported on TiO_2–CeO_2 mixed oxides for aqueous nitrate reduction by hydrogen, J. Mol. Catal. A Chem. 392 (2014) 308–314, https://doi.org/10.1016/j.molcata.2014.05.034.

[34] M. Yue, M. Cui, N. Zhang, Z. Long, X. Huang, Characterization of CeO2-ZrO2 mixed oxides prepared by two different co-precipitation methods, J. Rare Earths 31 (3) (2013) 251, https://doi.org/10.1016/S1002-0721(12)60267-1.

[35] E. Trusova, A. Khrushcheva, K. Vokhmintcev, Sol–gel synthesis and phase composition of ultrafine ceria-doped zirconia powders for functional ceramics, J. Eur. Ceram. Soc. 32 (2012) 1977–1981, https://doi.org/10.1016/j.jeurceramsoc.2011.11.006.

[36] P. Scherrer, Bestimmung der Grösse und der inneren Struktur von Kolloidteilchen mittels Röntgensrahlen [Determination of the size and internal structure of colloidal particles using X-rays]. Nachr Ges Wiss Goettingen, Math-Phys Kl. 26 (1918) 98–100. German.

[37] C. Wagner, E. Davis, M. Zeller, J. Taylor, R. Raymond, L.H. Gale, Empirical atomic sensitivity factors for quantitative analysis by electron spectroscopy for chemical analysis, Surf. Interace Anal 3 (1981) 211–225.

[38] M. Jaworski, I. Lick, G. Siri, M. Casella, ZrO2-modified Al2O3-supported PdCu catalysts for the water denitrification reaction, Appl. Catal. B 156-157 (2014) 53–61, https://doi.org/10.1016/j.apcatb.2014.02.048.

[39] S. Mukherjee, V. Bedekar, A. Patra, P. Sastry, A. Tyagi, Study of agglomeration behavior of combustion-synthesized nano-crystalline ceria using new fuels, J. Alloys. Compd. 446 (2008) 493–497, https://doi.org/10.1016/j.jallcom.2007.11.070.

[40] M. Thommes, K. Kaneko, A.V. Neimark, J.P. Olivier, F. Rodriguez-Reinoso, J. Rouquerol, K.S.W. Sing, Physisorption of gases, with special reference to the evaluation of surface area and pore size distribution (IUPAC Technical Report), Pure Appl. Chem. 87 (2015) 1051–1069.

[41] A. Badri, C. Binet, J. Lavalley, An FTIR study of surface ceria hydroxy groups during a redox process with H2, J. Chem. SOC., Faraday Trans. 23 (1996) 4669–4673, https://doi.org/10.1039/FT9969204669.

[42] M. Dos Santos, R. Lima, C. Riccardi, R. Tranquilin, P. Bueno, J. Varela, E. Longo, Preparation and characterization of ceria nanospheres by microwave-hydrothermal method, Mater. Lett. 62 (2008) 4509–4511, https://doi.org/10.1016/j.matlet.2008.08.011.

[43] A. Trovarelli, Catalytic properties of Ceria and CeO2-Containing materials, Catal. Rev. 38 (4) (1996) 439–520, https://doi.org/10.1080/01614949608006464.

[44] S. Li, H. Zhang, Y. Dan, J. Deng, J. Wang, L. Xiong, Y. Chen, Design and synthetize highly active Pd-only three-way catalyst by optimizing the reducibility of CeO2-ZrO2-Al2O3 support, Mol. Catal. (2019), https://doi.org/10.1016/j.mcat.2019.110696.

[45] T. Taniguchi, N. Watanabe, A. Sugiyama, H. Subramani, N. Wagata, Matsushita, M. Yoshimura, Identifying defects in ceria-based nanocrystals by UV resonance raman, J. Phys. Chem. C 113 (46) (2009) 19789–19793, https://doi.org/10.1021/jp9049457.

[46] R. Crisostomo, R. Neto, M. Schmal, Synthesis of CeO_2 and $CeZrO_2$ mixed oxide nanostructured catalysts for the iso-syntheses reaction, Appl. Catal. A Gen. 450 (2013) 131–142, https://doi.org/10.1016/j.apcata.2012.10.002.

[47] L. Lan, C. Yan, S. Chen, H. Li, D. Li, J. Wang, Y. Cheng, Y. Chen, Designed synthesis of semi-embedded Pd over CeO_2 -ZrO_2 /Al_2O_3 as advanced three-way catalyst, J. Taiwan Inst. Chem. Eng. (2018), https://doi.org/10.1016/j.jtice.2017.12.022.

[48] F. Zhang, Peng Wang, J. Koberstein, S. Khalid, Siu-Wai Chan, Cerium oxidation state in ceria nanoparticles studied with X-ray photoelectron spectroscopy and absorption near edge spectroscopy, Surface Sci 563 (2004) 74–82.

[49] N. Zhang, Y. Xu, Aggregation- and Leaching-Resistant, Reusable, and Multifunctional Pd@CeO_2 as a Robust Nano catalyst Achieved by a Hollow Core–Shell Strategy, Chem. Mater. 25 (2013) 1979–1988, https://doi.org/10.1021/cm400750c.

[50] Y. Lei, W. Li, Q. Liu, Q. Lin, X. Zheng, Q. Huang, S. Guan, X. Wang, C. Wang, F. Li, Typical crystal face effects of different morphology ceria on the activity of Pd/CeO_2 catalysts for lean methane combustion, Fuel 233 (2018) 10–20, https://doi.org/10.1016/j.fuel.2018.06.035.

[51] A. Galtayries, R. Sporken, J. Riga, G. Blanchard, R. Caudano, XPS comparative study of ceria/zirconia mixed oxides: powders and thin film characterization, J. Electron Spectros. Relat. Phenomena 951 (1998) 88–91, https://doi.org/10.1016/S0368-2048(97)00134-5.

[52] Y. Gao, Y. Masuda, H. Ohta, K. Koumoto, Room-temperature preparation of ZrO_2 precursor thin film in an aqueous peroxozirconium-complex solution, Chem. Mater. 16 (2004) 2615–2622, https://doi.org/10.1021/cm049771i.

[53] M. Brun, A. Berthet, J. Bertolini, XPS, AES and Auger parameter of Pd and PdO, J. Electron Spectros. Relat. Phenomena 104 (1999) 55–60, https://doi.org/10.1016/S0368-2048(98)00312-0.

[54] D. Zemlyanov, B. Aszalos-Kiss, E. Kleimenov, D. Teschner, S. Zafeiratos, M. Havecker, A. Knop-Gericke, R. Schlögl, H. Gabasch, W. Unterberger, K. Hayek, B. Klötzer, Surf. Sci. 600 (2006) 983–994, https://doi.org/10.1016/j.susc.2005.12.020.

[55] H. Gabasch, W. Unterberger, K. Hayek, B. Klotzer, E. Kleimenov, D. Teschner, S. Zafeiratos, M. Havecker, A. Knop-Gericke, R. Schlogl, J. Han, F. Ribeiro, B. Aszalos-Kiss, T. Curtin, D. Zemlyanov, *In situ* XPS study of Pd(1 1 1) oxidation at elevated pressure, Part 2: palladium oxidation in the 10^{-1} mbar range, Surf. Sci. 600 (2006) 2980–2989, https://doi.org/10.1016/j.susc.2006.05.029.

[56] W. Epling, G. Hoflund, Catalytic oxidation of methane over ZrO_2-Supported Pd catalysts, J. Catal. 182 (1999) 5–12, https://doi.org/10.1006/jcat.1998.2341.

[57] K. Priolkar, P. Bera, P. Sarode, M. Hegde, S. Emura, R. Kumashiro, N. Lalla, Formation of $Ce_{1-x}Pd_xO_{2-\delta}$ Solid Solution in Combustion-Synthesized Pd/CeO_2 Catalyst: XRD, XPS, and EXAFS Investigation, Chem. Mater. 14 (2002) 2120–2128, https://doi.org/10.1021/cm0103895.

[58] A. Devadas, S. Vasudevan, F. Epron, Nitrate reduction in water: influence of the addition of a second metal on the performances of the Pd/CeO(2) catalyst, J. Hazard. Mater. 185 (2-3) (2010) 1412–1417, https://doi.org/10.1016/j.jhazmat.2010.10.063.

[59] Y. Wei, J. Liu, Z. Zhao, A. Duan, G. Jiang, The catalysts of three-dimensionally ordered macroporous Ce1_xZrxO_2-supported gold nanoparticles for soot combustion: the metal–support interaction, J. Catal. 287 (2012) 13–29, https://doi.org/10.1016/j.jcat.2011.11.006.

[60] X. Yang, H. Bai, M. Qian, C. Wu, S. Cao, Z. Yan, Q. Tian, Z. Du, Enhanced activity of Pd–Cu(Ni) bimetallic catalysts for oxidative carbonylation of phenol, Mater. Chem. Phys. 234 (2019) 48–54, https://doi.org/10.1016/j.matchemphys.2019.05.049.

[61] N. Babu, N. Lingaiah, P. Prasad, Characterization and reactivity of Al_2O_3 supported Pd-Ni bimetallic catalysts for hydrochlorination of chlorobenzene, Appl. Catal. B 111–112 (2012) 309–316, https://doi.org/10.1016/j.apcatb.2011.10.013.

[62] Q. Wang, W. Wang, B. Yan, W. Shi, F. Cui, C. Wang, Well-dispersed Pd-Cu bimetals in TiO_2 nanofiber matrix with enhanced activity and selectivity for nitrate catalytic reduction, Chem. Eng. J. 326 (2017) 182–191, https://doi.org/10.1016/j.cej.2017.05.110.

[63] Z. Zhang, Y. Luo, Y. Guo, W. Shi, W. Wang, B. Zhang, R. Zhang, X. Bao, S. Wu, Cui. Pd and Pt nanoparticles supported on the mesoporous silica molecular sieve SBA-15 with enhanced activity and stability in catalytic bromate reduction, Chem. Eng. J. 344 (2018) 114–123, https://doi.org/10.1016/j.cej.2018.03.056.

[64] F. Marchesini, S. Irusta, C. Querini, E. Miró, Spectroscopic and catalytic characterization of Pd–In and Pt–In supported on Al_2O_3 and SiO_2, active catalysts for nitrate hydrogenation, Appl. Catal. A Gen. 348 (2008) 60–70, https://doi.org/10.1016/j.apcata.2008.06.026.

[65] O. Ilinitch, L. Nosova, V. Gorodetskii, V. Ivanov, S. Trukhan, E. Gribov, S. Bogdanov, F. Cuperus, Catalytic reduction of nitrate and nitrite ions by hydrogen: investigation of the reaction mechanism over Pd and Pd–Cu catalysts, J. Mol. Catal. A Chem. 158 (2000) 237–249.

[66] Y. Yoshinaga, T. Akita, I. Mikami, T. Okuhara, Hydrogenation of nitrate in water to nitrogen over Pd–Cu supported on active carbon, J. Catal. 207 (2002) 37–45, https://doi.org/10.1006/jcat.2002.3529.

[67] O. Soares, P. Ramalho, A. Fernandes, J. Órfao, M. Pereira, Catalytic bromate reduction in water: influence of carbon support, J. Environ. Chem. Eng. 7 (2019) 103015, https://doi.org/10.1016/j.jece.2019.103015.

[68] J. Restivo, O. Soares, J. Órfao, M. Pereira, Catalytic reduction of bromate over monometallic catalysts on different powder and structured supports, Chem. Eng. J. 309 (2017) 197–205, https://doi.org/10.1016/j.cej.2016.10.025.

[69] G. Bond, Heterogeneous Catalysis: Principles and Applications, 2o Ed, University Press, Oxford, 1987.

[70] J. Zhou, X. Zhou, L. Li, Q. Chen, Enhanced liquid phase catalytic hydrogenation reduction of bromate over Pd-on-Au bimetallic catalysts, Appl. Catal. A Gen. (2018), https://doi.org/10.1016/j.apcata.2018.06.009.

[71] F. Epron, F. Gauthard, J. Barbien, Catalytic reduction of nitrate in water on a monometallic. Pd/CeO, J. Catal. 206 (2002) 363–367, https://doi.org/10.1006/jcat.2001.3498.